Science Advances
AAAS

Supplementary Materials for

STEM in situ thermal wave observations for investigating thermal diffusivity in nanoscale materials and devices

Hieu Duy Nguyen *et al.*

Corresponding author: Naoyuki Kawamoto, kawamoto.naoyuki@nims.go.jp

Sci. Adv. **10**, eadj3825 (2024)
DOI: 10.1126/sciadv.adj3825

The PDF file includes:

Other Supplementary Material for this manuscript includes the following:

Supplementary Text

Dependence of thermal waves on the tips of the thermocouple

In thermal measurements requiring physical contact, the method's accuracy is often questioned due to the stability of constant contact resistance. Moreover, it is critical to evaluate how quickly a thermocouple can respond to the heating effect of a pulsed electron beam. Our experiments have demonstrated that thermocouples with a diameter of the contact probe's tip of approximately 100-300 nm or less can achieve relatively similar response time and shape of thermal waves despite inevitable differences, such as thermal contact resistance between the thermocouple and the specimen, contact condition of chromel and constantan probes, and electron beam current (Fig. S2). A thermocouple with a diameter of any component larger than those sizes produces inferior performance due to fast thermal loss towards the cold side. Additionally, the shape of thermal waves appears nearly trapezoidal waves when f = 333 Hz and gradually turns into triangular waves with increasing modulated frequency (Fig. S2).

Effects of amorphous layer on the thermal diffusivity of the single-crystalline sapphire specimen

It is well-known that under the bombardment of Ga-ion beam, the surface of the FIB-microfabricated specimen usually suffers from the Ga-ion implantation, amorphization, and lattice distortion. First, we considered the effect of the amorphous aluminium oxide layer on the thermal diffusivity of the specimen. As shown in Fig. S7, there is an amorphous layer whose thickness is approximately several nm. The thermal diffusivity of amorphous aluminium oxide layers in the range of 2 - 490 nm was quantitatively determined in Ref. 57. Due to the size effect, the thermal diffusivity of amorphous layer with the thickness of 5 nm is about 0.35×10^{-6} m^2/s. Despite the size effect due to phonon scatterings at the specimen boundaries, since the thermal transport was still in a diffusive/Fourier regime, we could use the parallel model to determine effective thermal diffusivity as follows,

$$\alpha_{effective} = v_1\alpha_1 + v_2\alpha_2,$$

where α_1, α_2 are thermal diffusivity of components 1 and 2, respectively, and v_1, v_2 are volume fractions of components 1 and 2, respectively (*58*).

Applying the above model to the discussion, we regard the α_1, α_2 thermal diffusivity of single-crystalline sapphire and that of amorphous sapphire layer, respectively. Assuming the thickness of the total amorphous layer (surrounding the specimen) is about 10 nm along the single-crystalline sapphire specimen (the width and thickness of the specimen are equally ~430 nm), and the determined thermal diffusivity (6.87×10^{-6} m^2/s) is the effective thermal diffusivity of the specimen, we calculated the thermal diffusivity of single-crystalline sapphire component as 7.03×10^{-6} m^2/s. This value is obviously not the thermal diffusivity of single-crystalline sapphire (~10.8×10^{-6} m^2/s). As a result, the amorphous layers are not the factor causing the reduction of thermal diffusivity.

In the same manner, the thin Ga layer should not have significant impact on the total thermal diffusivity of the specimen. Therefore, the reduction of thermal diffusivity reported in the current study should be mainly attributed to the size effect.

Effects of voids on phase delay and amplitude of thermal waves

In Fig. 4, the effect of voids is investigated by acquiring a map of phase delay and a map of amplitude corresponding to the enlarged area (2). Smaller values of the amplitude of thermal waves are detected when electron beams scan through this void. According to Eq. (6), the possible reason for the change in amplitude is the change in absorbed thermal energy due to smaller thicknesses.

Additionally, a thin Ga layer is coated all around the specimen as an artifact of FIB microfabrication, and the thermal waves induced by electron beam irradiated on both AlN and Ga. This evidence infers that, at the void, thermal waves are more likely to be affected by the combined thermal waves due to the smaller thickness of AlN, which also explains the decrement of phase delay at the void. Without the presence of a Ga layer, according to Eq. (5), there should be no change in contrast at the void area in the map of phase delay, as the phase delay is independent of the specimen thickness. Similarly, the results of phase delay and amplitude can be interpreted with the inclined edge area on the left side of the specimen.

Phase-spatial resolution

The nominal phase resolution of the lock-in amplifier is 0.001°. The phase-spatial resolution depends on modulated frequencies of pulsed convergent electron beam and the thermal diffusivity of the material. Assuming the modulated frequencies of the pulsed convergent electron beam as 5, 10, 20, and 100 kHz, and the thermal diffusivity of the unknown material is 10^{-4}, 10^{-5}, 10^{-6}, and 10^{-7} m^2/s, respectively, the corresponding ideal phase-spatial resolutions of the measurements are calculated using Eq. S5 and shown in the below table

Table. S1 Ideal phase-spatial resolutions of the measurements in nm

		Modulated frequencies of the pulsed convergent electron beam (kHz)			
		5	**10**	**20**	**100**
Thermal diffusivity (m^2/s)	**10^{-4}**	139.3	98.5	69.6	31.1
	10^{-5}	44.0	31.1	22.0	9.8
	10^{-6}	13.9	9.8	7.0	3.1
	10^{-7}	4.4	3.1	2.2	1.0

The ideal phase-spatial resolution increases with increasing modulated frequencies of pulsed convergent electron beam and decreasing thermal diffusivity. However, the upper limit of the ideal phase-spatial resolution depends on the diameter of the convergent electron beam. In the present study, the diameter of the electron beam is approximately 2-3 nm. Therefore, in the present study, the phase-spatial resolution is limited by 2-3 nm.

In practice, the obtained phase delay during the measurements is affected by several factors, such as the sensitivity and the time constant of the lock-in amplifier. The sensitivity was set up automatically on the lock-in amplifier. The time constant was set up so that the phase delay at each position was stable. As the time constant controls the ability to eliminate signals having frequencies other than that of the thermal waves (which is also the modulated frequency), the longer the time constant is, the narrower the band of allowed frequencies becomes. With a narrower band of allowed frequencies, the phase delay of thermal waves is read more correctly due to the elimination of signals with undesired frequencies, enhancing phase-spatial resolution. However, the trade-off is the requirement of longer exposure time for each pixel. Otherwise, the obtained map of phase delay will be shifted compared to the HAADF-STEM image. To reduce the total time for each mapping image, the magnification and the number of pixels can be varied to balance the quality of the image of interest and the recording time. A recording time that is too long may cause the drifting of the specimen and ruin the image. In the present study, the result of

phase delays of single-crystalline sapphire specimen was recorded with a time constant of 10 ms and exposure time of 20 ms, and the result of phase delays of polycrystalline AlN specimen was recorded with a time constant of 100 ms and exposure time of 101 ms. The selection of a short time constant for the case of single-crystalline sapphire specimen is justified by the unnecessity of a long time constant since no information on nanostructures is supposed to be observed. In contrast, for the case of polycrystalline AlN specimen, a much longer time constant was utilized to visualize local thermal properties of nanostructures like grain boundaries and voids. Additionally, the modulated frequency of 100 kHz was adopted to enhance the phase-spatial resolution. As a much more severe attenuation of thermal waves at high frequencies required a sufficiently long time constant, a time constant of 100 ms was employed. Fig. S6 shows a phase-spatial resolution of ~10 nm with the settings mentioned earlier. A higher phase-spatial resolution can be achieved by further varying the number of pixels and magnification depending on the image of interest.

In general, the phase-spatial resolution is not constant but varies depending on the modulated frequency of pulsed convergent electron beam, the thermal diffusivity of the material, the selection of time constant of the lock-in amplifier, the magnification of TEM, and the number of pixels scanned by the electron beam. A good combination of the above factors provides an optimum set of conditions for investigating a specific specimen. To further improve the quality of the map of phase delay or map of amplitude of thermal waves, one should increase the beam current or decrease the acceleration voltage of the pulsed focused electron beam to increase the heating effect of the electron beam due to plasmon loss. However, the reduction of acceleration voltage reduces the TEM spatial resolution; thus, it should be carried out with consideration.

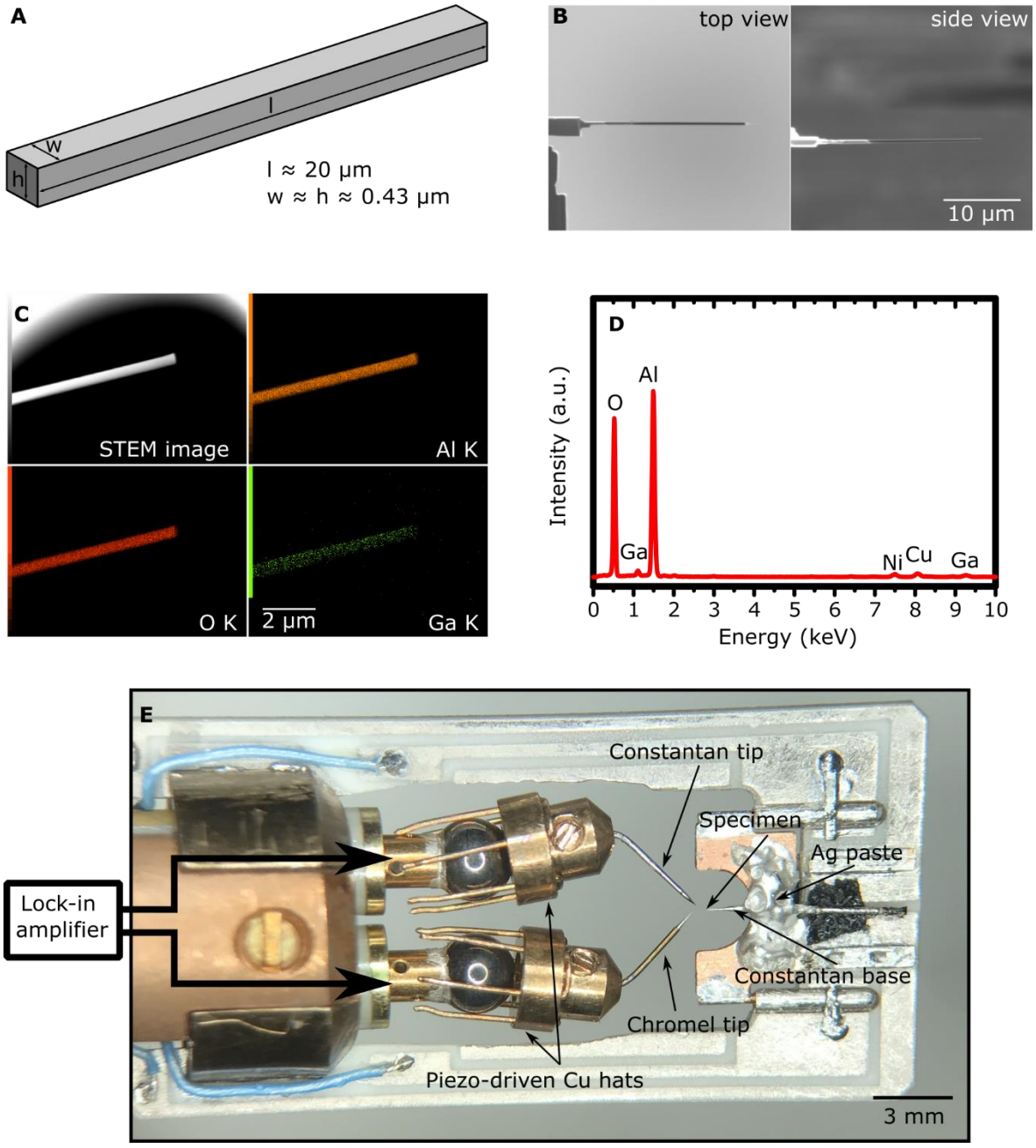

Fig. S1 Information on the specimen used in the present report and experimental setup. (A) Geometrical shape and dimensions of the single-crystalline sapphire specimen, **(B)** Scanning ion image of the top view and side view of the sapphire specimen, **(C)** Energy dispersive spectroscopy (EDS) mappings of the sapphire specimen. The residual Ga content is due to the artifact of FIB microfabrication. **(D)** The EDS spectrum of the specimen is shown in **(C)**; however, Ni and Cu stem from the thermocouple, which is near the specimen but not present in the frame of the image, **(E)** Experimental setup used in the present report (is also similar to the one used in Ref 23.)

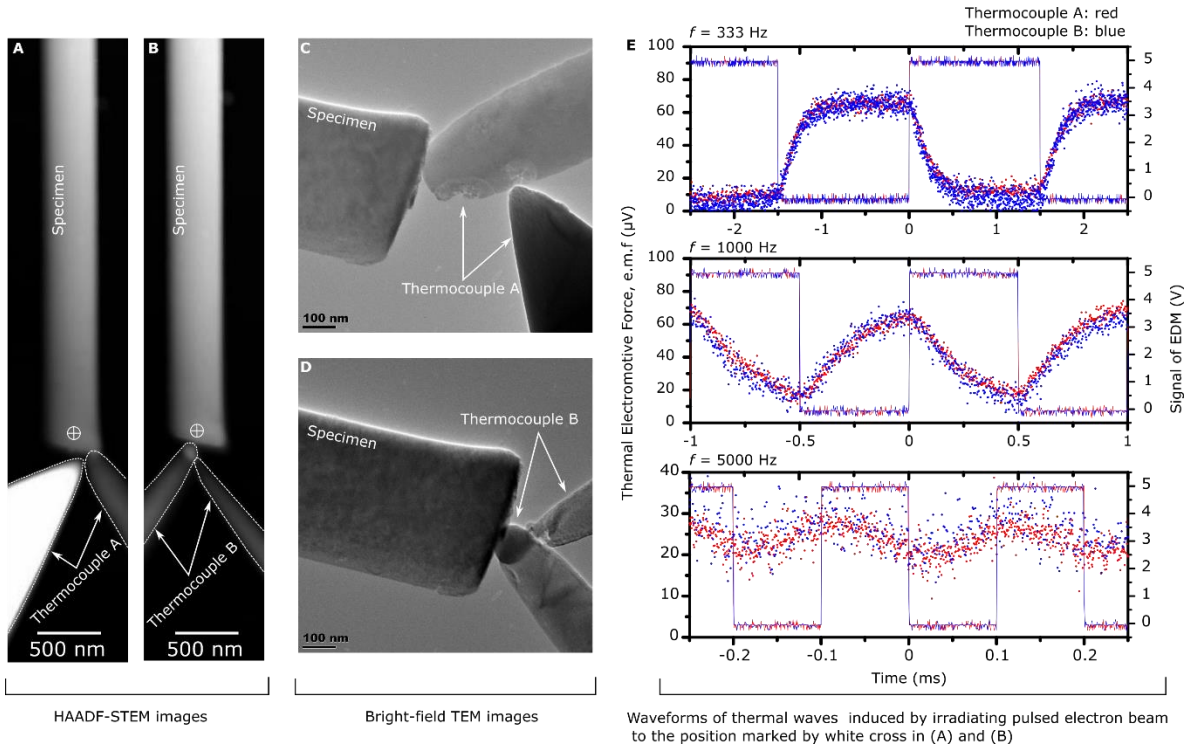

Fig. S2 Dependence of thermal waves on the size of the tips of the thermocouple. (A) and **(C)** are HAADF-STEM image and bright-field TEM image of experimental setup employing thermocouple A, respectively, **(B)** and **(D)** are HAADF-STEM image and bright-field TEM images of experimental setup employing thermocouple B, respectively. **(E)** Thermal waves induced by a pulsed focused electron beam under modulated frequencies of 333, 1000, and 5000 Hz from upper to lower are detected by thermocouple A (shown in red) and thermocouple B (shown in blue). Change in the size of the tips of the thermocouple almost does not affect the response time, amplitude, and shape of thermal waves. Deviation in the magnitude of thermal waves is easier to recognize when using thermocouple B. The difference in the impedance of the thermocouple junction (~600 Ω in thermocouple B vs. ~300 Ω in thermocouple A), which leads to a difference in thermal noise, is the reason for that deviation.

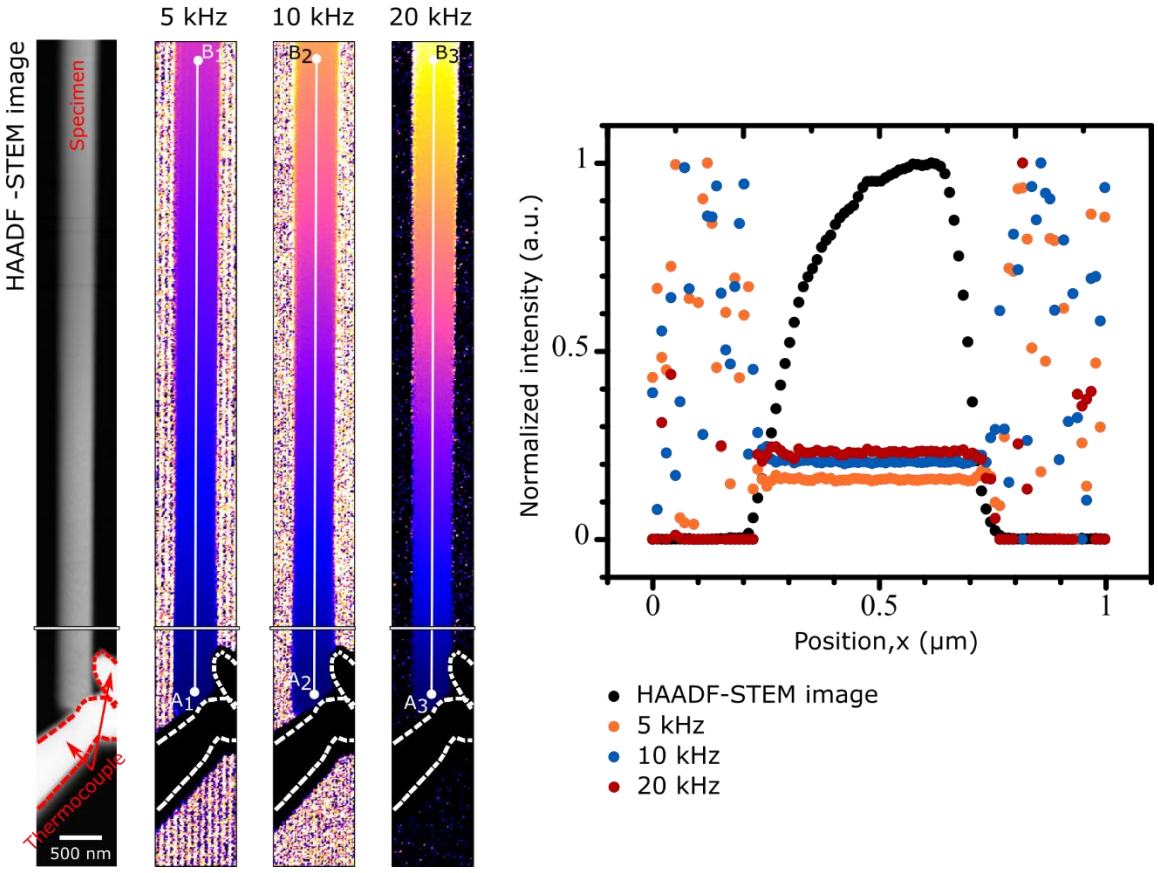

Fig. S3 The consistency of phase delay in the horizontal direction. Phase delay in the horizontal direction is nearly constant, as shown in the line profile on the right side. Outside of the specimen, the signal of phase delay is not detected. In this area, the phase is not locked by the lock-in-amplifier, which results in noise-like data. The consistency of the phase delay in the horizontal direction allows us to employ a one-dimensional heat transport equation with respect to the vertical direction for determining the thermal diffusivity of the specimen.

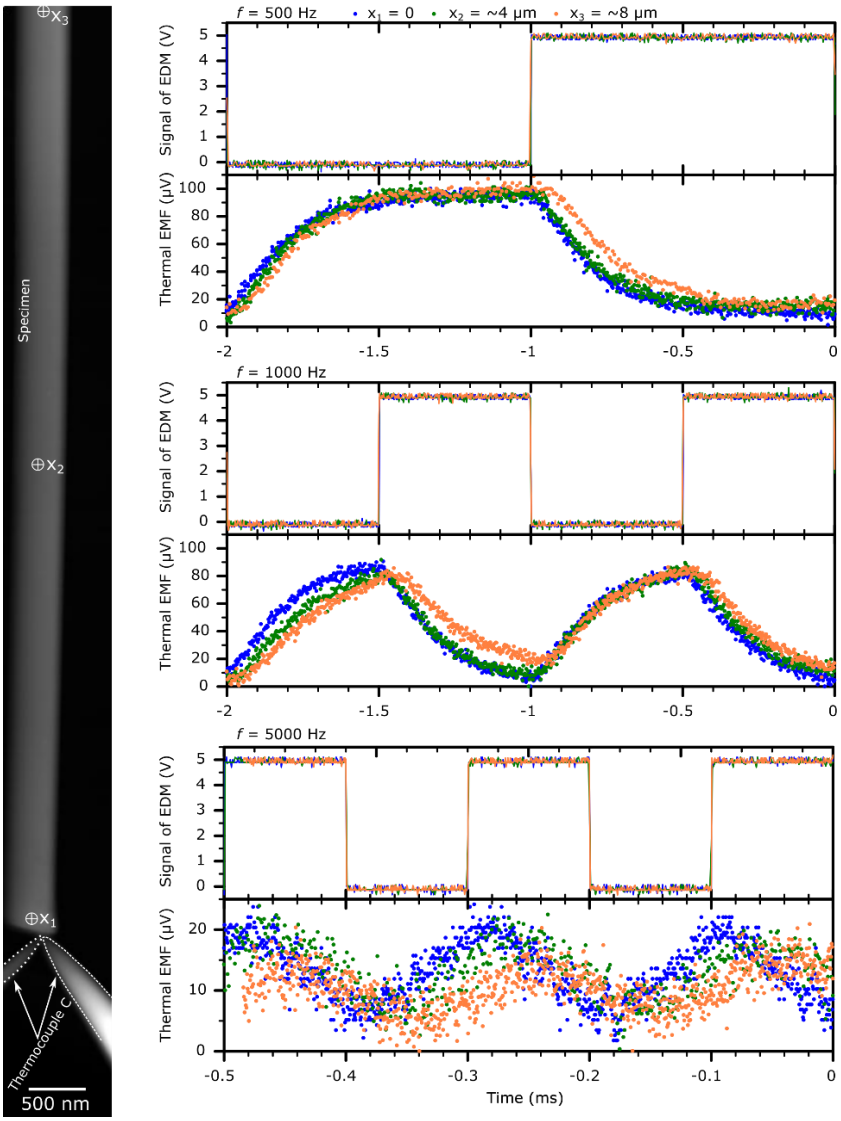

Fig. S4 Dependence of thermal wave on the distance. Thermal waves and signals of EDM were acquired by thermocouple C shown beside the HAADF-STEM image. From upper to lower, signals of EDM and correspondingly induced thermal waves at modulated frequencies of 500, 1000, and 5000 Hz were obtained near the thermocouple (blue), ~ 4 μm from the thermocouple (green), and ~ 8 μm from the thermocouple (orange). At all modulated frequencies, there is no temporal difference in signals of EDM. However, the thermal waves are visibly shifted to the right with increasing distance from the thermocouple, which verifies Eq. (5). Notably, despite the difference in phase delay, the rising time of the responded thermal signals hardly changes. This fact is essential to precisely evaluate the phase delay of thermal waves throughout the specimen.

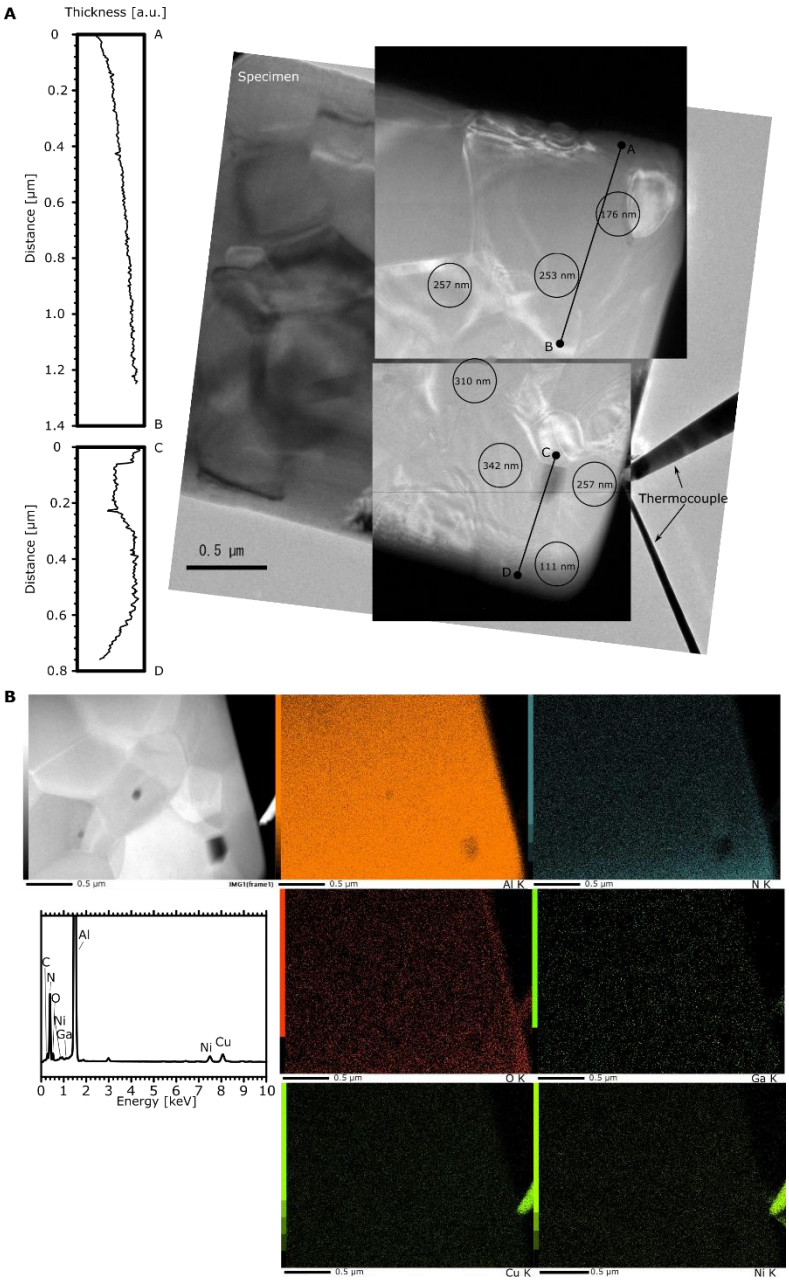

Fig. S5 Characterization of the polycrystalline AlN specimen. (A) Bright-field TEM image combined with thickness maps in corresponding areas. Thickness profiles along line AB and CD are shown in the left-side graphs. The thickness maps show the values of measurement of the specimen's thickness by EELS using the effective atomic number of AlN of 10.8. Thickness profiles indicate that the specimen does not have a uniform thickness, which is thinner at the upper area and thicker at the lower area. In addition, the edges of both the upper and lower areas are slightly inclined. The non-uniformity of thickness and the inclined edges are due to the FIB microfabrication. **(B)** The HAADF-STEM image is accompanied by elemental maps and the EDS result of the AlN specimen.

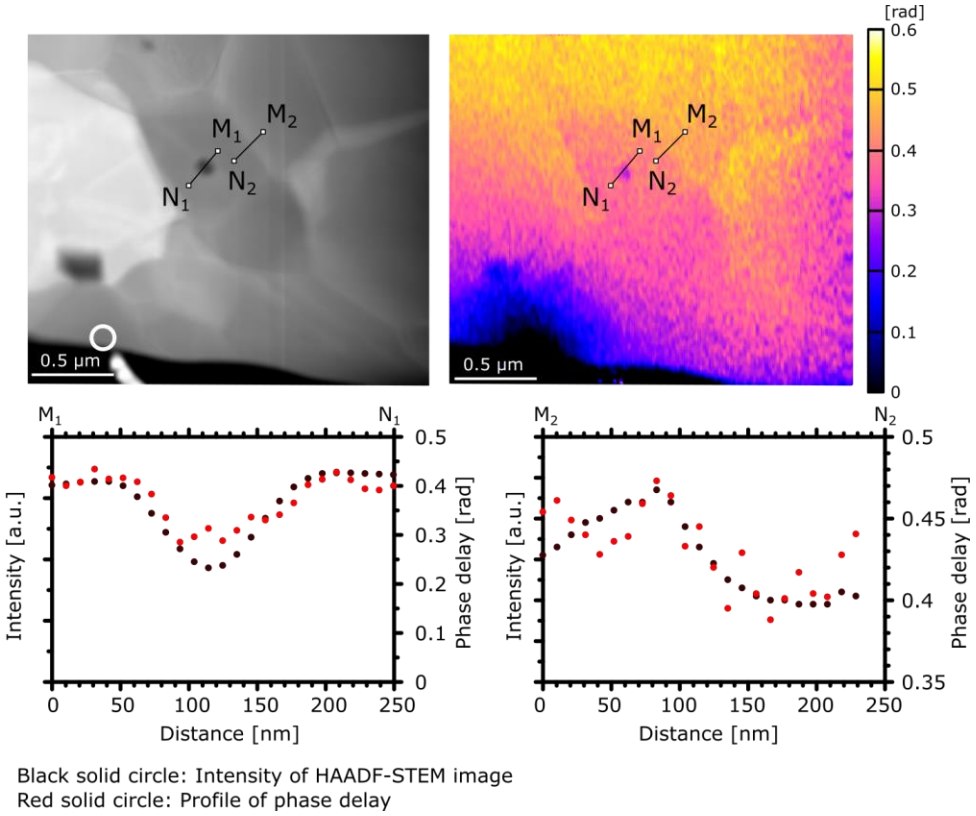

Fig. S6 Phase-spatial resolution under conditions of modulated frequency of 100 kHz, time constant of 100 ms, and exposure time of 101 ms/pixel. Comparison between line profiles of phase delay and intensity of STEM-HAADF image indicates a phase-spatial resolution of ~10 nm.

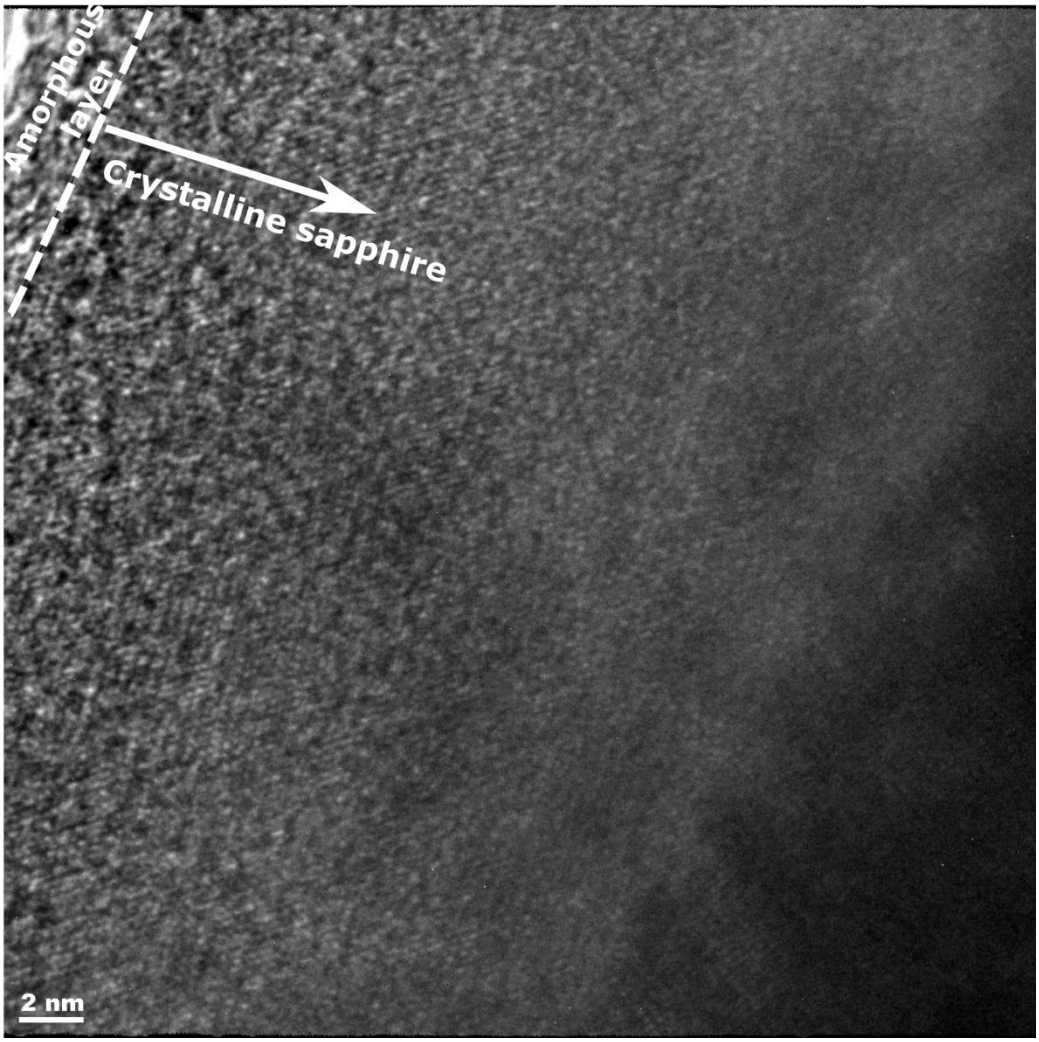

Fig. S7 Lattice TEM image of the single-crystalline sapphire specimen. The image was taken at the edge of the specimen showing a few-nanometer-thick amorphous layer due to the bombardment of Ga-ion beam during FIB-microfabrication.

Movie S1

Animation of transport of thermal waves inside the specimen of single-crystalline sapphire under modulated frequency of 5 kHz. The scale bar is 500 nm.

Movie S2

Animation of transport of thermal waves inside the specimen of single-crystalline sapphire under modulated frequencies of 10 kHz. The scale bar is 500 nm.

Movie S3

Animation of transport of thermal waves inside the specimen of single-crystalline sapphire under modulated frequencies of 20 kHz. The scale bar is 500 nm.

REFERENCES AND NOTES

1. Dave S. Steinberg, Preface in Ed. 3, *Vibration Analysis For Electronic Equipment* (Wiley-Interscience, ed. 3, 2000).

2. I. Ferain, C. A. Colinge, J.-P. Colinge, Multigate transistors as the future of classical metal–oxide–semiconductor field-effect transistors. *Nature* **479**, 310–316 (2011).

3. X.-L. Shi, J. Zou, Z.-G. Chen, Advanced thermoelectric design: From materials and structures to devices. *Chem. Rev.* **120**, 7399–7515 (2020).

4. R. Anufriev, J. Ordonez-Miranda, M. Nomura, Measurement of the phonon mean free path spectrum in silicon membranes at different temperatures using arrays of nanoslits. *Phys. Rev. B* **101**, 115301 (2020).

5. K. M. Hoogeboom-Pot, J. N. Hernandez-Charpak, X. Gu, T. D. Frazer, E. H. Anderson, W. Chao, R. W. Falcone, R. Yang, M. M. Murnane, H. C. Kapteyn, D. Nardi, A new regime of nanoscale thermal transport: Collective diffusion increases dissipation efficiency. *Proc. Natl. Acad. Sci. U.S.A.*. **112**, 4846–4851 (2015).

6. A. Sood, R. Cheaito, T. Bai, H. Kwon, Y. Wang, C. Li, L. Yates, T. Bougher, S. Graham, M. Asheghi, M. Goorsky, K. E. Goodson, Direct visualization of thermal conductivity suppression due to enhanced phonon scattering near individual grain boundaries. *Nano Lett.* **18**, 3466–3472 (2018).

7. J. Liu, H. Wang, Y. Hu, W. Ma, X. Zhang, Laser flash-Raman spectroscopy method for the measurement of the thermal properties of micro/nano wires. *Rev. Sci. Instrum.* **86**, 014901 (2014).

8. C. Li, S. Xu, Y. Yue, B. Yang, X. Wang, Thermal characterization of carbon nanotube fiber by time-domain differential Raman. *Carbon* **103**, 101–108 (2016).

9. L. Arnoldi, M. Spies, J. Houard, I. Blum, A. Etienne, R. Ismagilov, A. Obraztsov, A. Vella, Thermal diffusivity of diamond nanowires studied by laser assisted atom probe tomography. *Appl. Phys. Lett.* **112**, 143104 (2018).

10. A. Kumar, J. Bogdanowicz, J. Demeulemeester, J. Bran, D. Melkonyan, C. Fleischmann, W. Vandervorst, Measurement of the apex temperature of a nanoscale semiconducting field emitter illuminated by a femtosecond pulsed laser. *J. Appl. Phys.* **124**, 245105 (2018).

11. K. Kim, W. Jeong, W. Lee, P. Reddy, Ultra-high vacuum scanning thermal microscopy for nanometer resolution quantitative thermometry. *ACS Nano* **6**, 4248–4257 (2012).

12. F. Menges, P. Mensch, H. Schmid, H. Riel, A. Stemmer, B. Gotsmann, Temperature mapping of operating nanoscale devices by scanning probe thermometry. *Nat. Commun.* **7**, 10874 (2016).

13. S. Gonzalez-Munoz, K. Agarwal, E. G. Castanon, Z. R. Kudrynskyi, Z. D. Kovalyuk, J. Spièce, O. Kazakova, A. Patanè, O. V. Kolosov, Direct measurements of anisotropic thermal transport in γ-InSe nanolayers via cross-sectional scanning thermal microscopy. *Adv. Mater. Interfaces* **10**, 2300081 (2023).

14. D. Seto, R. Nikka, S. Nishio, Y. Taguchi, T. Saiki, Y. Nagasaka, Nanoscale optical thermometry using a time-correlated single-photon counting in an illumination-collection mode. *Appl. Phys. Lett.* **110**, 033109 (2017).

15. Q. Weng, K.-T. Lin, K. Yoshida, H. Nema, S. Komiyama, S. Kim, K. Hirakawa, Y. Kajihara, Near-field radiative nanothermal imaging of nonuniform Joule heating in narrow metal wires. *Nano Lett.* **18**, 4220–4225 (2018).

16. P.-I. Wang, Y. P. Zhao, G. C. Wang, T. M. Lu, Novel growth mechanism of single crystalline Cu nanorods by electron beam irradiation. *Nanotechnology* **15**, 218–222 (2004).

17. L. Shi, L. He, L. Shangguan, Y. Zhou, B. Wang, L. Zhang, Y. Yang, C. Teng, L. Sun, Revealing the phase segregation and evolution dynamics in binary nanoalloys via electron beam-assisted ultrafast heating and cooling. *ACS Nano* **16**, 921–929 (2022).

18. H. Guo, M. I. Khan, C. Cheng, W. Fan, C. Dames, J. Wu, A. M. Minor, Vanadium dioxide nanowire-based microthermometer for quantitative evaluation of electron beam heating. *Nat. Commun.* **5**, 4986 (2014).

19. M. Mecklenburg, A. H. William, E. R. White, R. Dhall, B. C. Stephen, S. Aloni, B. C. Regan, Nanoscale temperature mapping in operating microelectronic devices. *Science* **347**, 629–632 (2015).

20. X. Yan, C. Liu, C. A. Gadre, S. Dai, L. Gu, K. Yu, T. Aoki, R. Wu, X. Pan, Unexpected strong thermally induced phonon energy shift for mapping local temperature. *Nano Lett.* **19**, 7494–7502 (2019).

21. M. J. Lagos, P. E. Batson, Thermometry with subnanometer resolution in the electron microscope using the principle of detailed balancing. *Nano Lett.* **18**, 4556–4563 (2018).

22. J. C. Idrobo, A. R. Lupini, T. Feng, R. R. Unocic, F. S. Walden, D. S. Gardiner, T. C. Lovejoy, N. Dellby, S. T. Pantelides, O. L. Krivanek, Temperature measurement by a nanoscale electron probe using energy gain and loss spectroscopy. *Phys. Rev. Lett.* **120**, 095901 (2018).

23. N. Kawamoto, Y. Kakefuda, T. Mori, K. Hirose, M. Mitome, Y. Bando, D. Golberg, Visualizing nanoscale heat pathways. *Nano Energy* **52**, 323–328 (2018).

24. N. Kawamoto, Y. Kakefuda, I. Yamada, J. Yuan, K. Hasegawa, K. Kimoto, T. Hara, M. Mitome, Y. Bando, T. Mori, D. Golberg, Nanoscale characterization of the thermal interface resistance of a heat-sink composite material by *in situ* TEM, *Nanotechnology* **26**, 465705 (2015)

25. D. R. Lide, Section 4 in *CRC Handbook of Chemistry and Physics*, 85th Edition. (CRC Press, 2004), p. 4–39.

26. Y. S. Touloukian, R. W. Powell, C. Y. Ho, P. G. Klemens, *Thermophysical Properties of Matter Vol 2 Thermal Conductivity Nonmetallic Solids*. (IFI/Plenum, 1970), p. 94–97.

27. Y. S. Touloukian, E. H. Buyco, *Thermophysical properties of matter Vol 5 Specific Heat: Nonmetallic Solids*. (IFI/Plenum, 1970), pp. 26–29.

28. Y. Hu, L. Zeng, A. J. Minnich, M. S. Dresselhaus, G. Chen, Spectral mapping of thermal conductivity through nanoscale ballistic transport. *Nat. Nanotechnol.* **10**, 701–706 (2015).

29. D. G. Cahill, W. K. Ford, K. E. Goodson, G. D. Mahan, A. Majumdar, H. J. Maris, R. Merlin, S. R. Phillpot, Nanoscale thermal transport. *J. Appl. Phys.* **93**, 793–818 (2002).

30. A. J. Minnich, J. A. Johnson, A. J. Schmidt, K. Esfarjani, M. S. Dresselhaus, K. A. Nelson, G. Chen, Thermal conductivity spectroscopy technique to measure phonon mean free paths. *Phys. Rev. Lett.* **107**, 095901 (2011).

31. A. J. Minnich, Determining phonon mean free paths from observations of quasiballistic thermal transport. *Phys. Rev. Lett.* **109**, 205901 (2012).

32. C. Hua, A. J. Minnich, Transport regimes in quasiballistic heat conduction. *Phys. Rev. B* **89**, 094302 (2014).

33. P. Torres, M. Royo, M. López-Suárez, J. Shiomi, R. Rurali, Quasiballistic phonon transport from first principles. *Phys. Rev. B* **102**, 144305 (2020).

34. Y. D. Wilde, F. Formanek, R. Carminati, B. Gralak, P.-A. Lemoine, K. Joulain, J.-P. Mulet, Y. Chen, J.-J. Greffet, Thermal radiation scanning tunnelling microscopy. *Nature* **444**, 740–743 (2006).

35. M. J. Lagos, A. Trügler, U. Hohenester, P. E. Batson, Mapping vibrational surface and bulk modes in a single nanocube. *Nature* **543**, 529–532 (2017).

36. Y. Wu, J. Ordonez-Miranda, S. Gluchko, R. Anufriev, D. D. S. Meneses, L. D. Campo, S. Volz, M. Nomura, Enhanced thermal conduction by surface phonon-polaritons. *Sci. Adv.* **6**, eabb4461 (2020).

37. L. Tranchant, S. Hamamura, J. Ordonez-Miranda, T. Yabuki, A. Vega-Flick, F. Cervantes-Alvarez, J. J. Alvarado-Gil, S. Volz, K. Miyazaki, Two-dimensional phonon polariton heat transport. *Nano Lett.* **19**, 6924–6930 (2019).

38. W. Kim, Strategies for engineering phonon transport in thermoelectrics. *J. Mater. Chem. C.* **3**, 10336–10348 (2015).

39. A. T. Wieg, Y. Kodera, Z. Wang, C. Dames, J. E. Garay, Thermomechanical properties of rare-earth-doped AlN for laser gain media: The role of grain boundaries and grain size. *Acta Mater.* **86**, 148–156 (2015).

40. X. Wu, L. Tang, C. L. Hardin, C. Dames, Y. Kodera, J. E. Garay, Thermal conductivity and management in laser gain materials: A nano/microstructural perspective. *J. Appl. Phys.* **131**, 020902 (2022).

41. P. K. Kuo, G. W. Auner, Z. L. Wu, Microstructure and thermal conductivity of epitaxial AlN thin films. *Thin Solid Films* **253**, 223–227 (1994).

42. Y. Zhao, C. Zhu, S. Wang, J. Z. Tian, D. J. Yang, C. K. Chen, H. Cheng, P. Hing, Pulsed photothermal reflectance measurement of the thermal conductivity of sputtered aluminum nitride thin films. *J. Appl. Phys.* **96**, 4563–4568 (2004).

43. C. Duquenne, M. P. Besland, P. Y. Tessier, E. Gautron, Y. Scudeller, D. Averty, Thermal conductivity of aluminium nitride thin films prepared by reactive magnetron sputtering. *J. Phys. D* **45**, 015301 (2012).

44. R. L. Xu, M. M. Rojo, S. M. Islam, A. Sood, B. Vareskic, A. Katre, N. Mingo, K. E. Goodson, H. G. Xing, D. Jena, E. Pop, Thermal conductivity of crystalline AlN and the influence of atomic-scale defects. *J. Appl. Phys.* **126**, 185105 (2019).

45. G. Chen, Non-Fourier phonon heat conduction at the microscale and nanoscale. *Nat. Rev. Phys.* **3**, 555–569 (2021).

46. G. Wehmeyer, Modeling ballistic phonon transport from a cylindrical electron beam heat source. *J. Appl. Phys.* **126**, 124306 (2019).

47. K. L. Chopra, S. K. Bahl, M. R. Randlett, Thermopower in thin-film copper—Constantan couples. *J. Appl. Phys.* **39**, 1525–1528 (1968).

48. G. P. Szakmany, A. O. Orlov, G. H. Bernstein, W. Porod, Single-metal nanoscale thermocouples. *IEEE Trans. Nanotechnol.* **13**, 1234–1239 (2014).

49. M. C. Salvadori, A. R. Vaz, F. S. Teixeira, M. Cattani, I. G. Brown, Thermoelectric effect in very thin film Pt⁄Au thermocouples. *Appl. Phys. Lett.* **88**, 133106 (2006).

50. L. Scarioni, E. M. Castro, Thermoelectric power in thin film Fe–CuNi alloy (type-J) couples. *J. Appl. Phys.* **87**, 4337–4339 (2000).

51. N. W. Ashcroft, N. D. Mermin, Chapter 2 in *Solid State Physics* (Harcourt College, 1976), p. 52.

52. A. J. Angström, XVII. New method of determining the thermal conductibility of bodies. *Science* **25**, 130–142 (1863).

53. J. Morikawa, T. Hashimoto, Analysis of high-order harmonics of temperature wave for Fourier transform thermal analysis. *Jpn. J. Appl. Phys.* **37**, L1484 (1998).

54. L. Reimer, Chapter 10 in *Transmission Electron Microscopy* (Springer-Verlag, ed. 3, 1993), p. 435–438.

55. H. Meltzman, Y. Kauffmann, P. Thangadurai, M. Drozdov, M. Baram, D. Brandon, W. D. Kaplan, An experimental method for calibration of the plasmon mean free path. *J. Microsc.* **236**, 165–173 (2009).

56. Y. Kakefuda, N. Kawamoto, M. Mitome, I. Yamada, T. Mori, D. Golberg, Development of nanoscale thermocouple probes for local thermal measurements. *Surf. Sci. Nanotechnol.* **17**, 102–107 (2019).

57. A. A. Mohtar, G. Tessier, R. Ritasalo, M. Matvejeff, J. Stormonth-Darling, P. S. Dobson, P. O. Chapuis, S. Gomès, J. P. Roger, Thickness-dependent thermal properties of amorphous insulating thin films measured by photoreflectance microscopy. *Thin Solid Films* **642**, 157–162 (2017).

58. A. Salazar, A. Sánchez-Lavega, J. M. Terrón, Effective thermal diffusivity of layered materials measured by modulated photothermal techniques. *J. Appl. Phys.* **84**, 3031–3041 (1998).